AIAA 2013-2654

Envelope Protection for Contaminant-Induced Adverse Aerodynamics on a Wing Using Flap Hinge Moment Measurements

Phillip J. Ansell*
University of Illinois at Urbana-Champaign, Urbana, Illinois 61801

Michael F. Kerho†
Rolling Hills Research Corporation, El Segundo, California 90245

and

Michael B. Bragg‡
University of Illinois at Urbana-Champaign, Urbana, Illinois 61801

A hinge moment based stall prediction method originally designed using 2D airfoil data is extended to a 3D wing. Experimental hinge moment measurements were obtained for a NACA 3415 semispan wing model in a clean configuration and with various simulated leading-edge contaminants. The effects of the simulated contamination configurations on the 3D wing and approximate 2D sectional performance are presented. These unsteady hinge moment data were processed through three detector functions to provide envelope protection for the clean and contaminated wing. The envelope protection advisories predicted by the detector functions are shown to be effective in predicting the angle-of-attack boundary of the normal flight envelope across various flap setting configurations and contamination configurations for the wing. Moreover, the use of the envelope protection system on data obtained during an unsteady pitch maneuver suggests that the envelope protection system may also function effectively in a dynamic environment. These results establish the viability of using this method on a flight vehicle.

Nomenclature

c	=	local chord length
$\bar{c}$	=	mean aerodynamic chord
C_d	=	sectional drag coefficient
C_D	=	wing drag coefficient
C_h	=	sectional hinge moment coefficient
C_l	=	sectional lift coefficient
C_L	=	wing lift coefficient
C_m	=	sectional quarter-chord pitching moment coefficient
C_M	=	wing quarter-chord pitching moment coefficient
C_p	=	pressure coefficient
h	=	feature height
k	=	reduced frequency ($\omega\bar{c}/2U_\infty$)
M_∞	=	freestream Mach number
Re	=	Reynolds number based on mean aerodynamic chord
x	=	coordinate in the wing model chordwise direction
α	=	wing angle of attack

* Graduate Research Assistant, Department of Aerospace Engineering, Member AIAA.
† Chief Aerodynamicist, Associate Fellow AIAA.
‡ Professor of Aerospace Engineering, Interim Dean of College of Engineering, Fellow AIAA.

α_{crit} = angle-of-attack boundary of adverse aerodynamic flight envelope
α_{stall} = wing stall angle of attack
δ_f = flap deflection angle
ω = angular frequency of unsteady pitch

I. Introduction

Despite the continual advances made in aviation technology, aircraft loss of control (LOC) remains the contributing factor that results in the greatest number of fatalities in commercial-jet flight worldwide.[1] As discussed by Wilborn and Foster,[2] aircraft LOC can be quantitatively defined using five flight envelopes related to various aspects of the aircraft system. According to these authors, aircraft LOC has been shown to occur when the boundaries of three of these five envelopes are exceeded. However, in the vehicle upset classification of LOC accidents, the leading contributing factor in loss of control accidents and fatalities is stall.[3] This type of event would most commonly occur when the bounds of the adverse aerodynamics envelope, as defined in Wilborn and Foster,[2] is exceeded. In order to continue with decreases in the annual aircraft accident rate across all classifications of flight, improved protection of aircraft flight envelopes is necessary.

Stall warning on a conventional, fixed-wing aircraft is commonly provided through a simple angle-of-attack system, composed of a pivoting vane element and supporting equipment. For such systems, the angle of attack can be measured, and a stall warning is provided when a pre-programmed threshold in α is reached. However, the dangers of stall can be unwittingly approached in the presence of adverse environmental conditions or insufficient situational awareness of the flight crew to the state of the aircraft. Under such circumstances, a stall warning or envelope protection system must be capable of adapting to changing conditions.

For example, Busch et al.[4] tested the effects of a horn-ice shape on an NACA 23012 airfoil model, discovering that the addition of the ice shape led to a reduction in $C_{l,max}$ of 55%, a reduction of α_{stall} by 50%, and increases in C_d by approximately 400%. Traditional angle-of-attack systems, like those mentioned previously, compensate for the ice-induced reductions in maximum lift and stall angle of attack by reducing the angle of attack at which a stall warning would be provided when the icing protection system is turned on. While the angle-of-attack reduction is highly aircraft dependent, conventional angle-of-attack systems on business jets are programmed to reduce the angle of attack where the stall warning is provided by approximately 3-5 degrees when the icing protection system is engaged.[5] In the case of a severe horn-ice shape, this reduction in angle of attack at which stall warning is provided could be insufficient.

Reductions in stall angle of attack are also not limited to icing conditions. Premature stall can occur due to other environmental contaminants, such as rain, frost, or distributed surface roughness. For example, Luers and Haines[6] identified a reduction in maximum lift by upwards of 30% for an aircraft in heavy rain conditions. Broeren and Bragg[7] also identified significant reductions in maximum lift for various airfoils with distributed leading-edge roughness.

In an effort to improve the current state of stall prediction and envelope protection for aircraft under adverse conditions, Gurbacki and Bragg[8] proposed a stall-prediction system for iced airfoils based on unsteady flap hinge moment measurements. These authors tested a NACA 23012 airfoil with a simple flap under clean and simulated glaze-iced configurations. For the iced case, as stall was approached, the ice-induced separated flow in the airfoil flowfield increased the amount of unsteadiness present in the hinge moment measurements, as evaluated by the hinge moment signal RMS, which was not present in the clean airfoil configuration. As a result, a correlation was discovered between the ice-induced separated flow prior to stall and the increase in unsteadiness in hinge moment measurements, and it was proposed that the unsteady hinge moment measurements could be used to predict ice-induced stall.[9] This stall prediction method was also proposed to be used as a part of Smart Icing Systems.[10]

A later study performed under a NASA Dryden sponsored Phase I and Phase II STTR with Rolling Hills Research Corporation and the University of Illinois[11,12,13] applied the original concept of Gurbacki and Bragg,[8] and developed a stall prediction system for airfoils in clean or contaminated configurations based solely on hinge moment measurements. These authors tested two airfoil models (a NACA 3415 and a NACA 23012) with a simple flap under an array of simulated contaminants. A reduction system was developed for these hinge moment measurements that provided a consistent stall prediction across most simulated contamination configurations. This reduction system is currently pending US Patent.

With the success of the hinge moment based stall prediction system for flapped 2D airfoil sections, it is desirable to understand how such a system could be applied to an aircraft. For this reason, the current study seeks to investigate the use of a hinge moment based envelope protection system on a 3D wing system with multiple flaps.

II. Experimental Methods

Wind Tunnel Data Acquisition

All data in the current investigation were acquired in the 3-ft × 4-ft wind tunnel at the University of Illinois at Urbana-Champaign. The wind tunnel has a maximum test section velocity of approximately 165 mph (242 ft/sec) and a freestream turbulence intensity under 0.1% for all operating speeds. The maximum streamwise Reynolds number is approximately 1.5×10^6/ft.

All measurements were acquired on a straight, tapered semispan wing model with a constant NACA 3415 cross-section across the entire semispan. A photograph of the model installed in the wind tunnel test section is presented in Fig. 1. The wing model had a semispan of 1.96 ft, a taper ratio of 0.7, and a resulting mean aerodynamic chord ($\bar{c}$) of 0.577 ft. The model was divided into three spanwise sections, which were denoted as the inboard, midspan, and outboard sections. Each section had a trailing-edge simple flap composing the aft 25% of the local chord. Each of the three flaps could be adjusted independently. All three spanwise sections also had a chordwise row of 32 pressure taps, from which the sectional performance was determined. This resulted in a total of 96 pressure taps on the model. Measurements were obtained for a Reynolds number of 0.7×10^6 ($M_\infty = 0.18$), based on the wing $\bar{c}$, for an array of different flap deflections and contamination configurations.

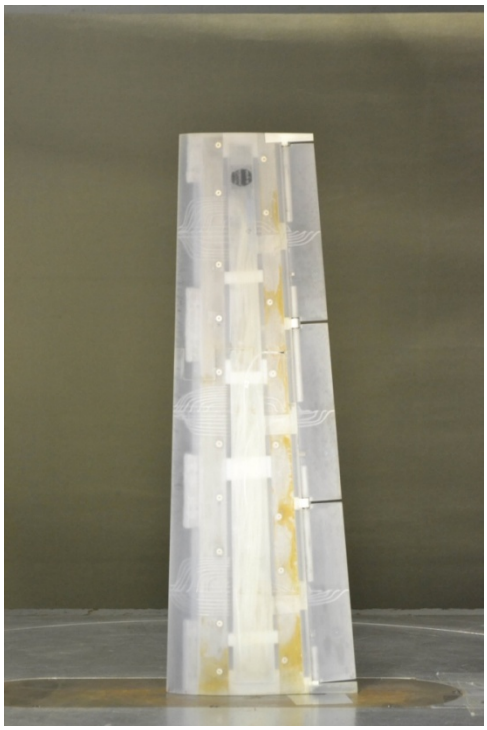

Fig. 1. Photograph of NACA 3415 wing model mounted in wind tunnel test section.

All steady pressure measurements, including both model and wake pressures, were obtained using an electronically-scanned pressure system. A three-component balance located under the wind tunnel test section was used to acquire the wing model lift, drag, and pitching moment performance, and had a turntable that was used to regulate the model angle of attack. Wake pressure profiles were obtained using a traversable wake rake located downstream of the wing model. Separate profiles were acquired for each spanwise section, directly downstream of the corresponding tap row.

Each flap had a strain gage instrumented control horn, which was used to acquire unsteady hinge moment measurements for the corresponding spanwise section. The model was also built with an accelerometer integrated near the tip of the wing and an unsteady pressure transducer integrated into the upper surface, just upstream of the midspan flap. Tests were performed for six different flap setting configurations. These configurations are summarized in Table 1. From Table 1, the flap configurations were designated by the notation of Inbord δ_f : Midspan δ_f : Outboard δ_f. This same notation will be used throughout the remainder of this paper.

All unsteady data were acquired simultaneously using a National Instruments SCXI sampling system. Unsteady measurements were sampled at a rate of 3 kHz for 10 seconds. Steady model pressure and wake data were used to

estimate the sectional performance about the center of each spanwise section. The surface static C_p distribution was integrated to obtain C_l and C_m for each spanwise section, and standard velocity deficit methods were used with the sectional wake profiles to obtain C_d for each spanwise section.

Flap Configuration	Inbord δ_f : Midspan δ_f : Outboard δ_f
1	0°:0°:0°
2	5°:5°:5°
3	-5°:-5°:-5°
4	0°:5°:0°
5	0°:-5°:0°
6	0°:0°:5°

Table 1. Flap configuration designations.

After reducing the wing and sectional forces and moments to coefficient form, wind tunnel corrections were applied to the coefficients. Standard three-dimensional corrections due to solid blockage, wake blockage, and streamline curvature were calculated for the wing performance coefficients and angle of attack using methods from Barlow et al.[14] In addition to correcting the 3D wing coefficients, corrections were also made to the sectional performance coefficients. However, there is not a standard method for determining wind tunnel corrections to be applied to sectional performance coefficients on a three-dimensional wing. As a result, the sectional performance coefficients were corrected using modifications of existing methods for wind tunnel corrections.

The sectional performance coefficients were first corrected by the solid blockage of the wing using the standard 3D corrections from Barlow et al.[14] The 3D variant of the solid blockage corrections were used, as the net flow acceleration in the test section due to solid blockage was due to the physical presence of the wing. The sectional performance coefficients were also corrected for wake blockage using the 2D correction factor from Barlow et al.[14] The 2D variant of the wake blockage corrections were used to correct the sectional performance data, as the amount of wake blockage was non-uniform across the wing semispan.

The final correction that was applied to the sectional performance coefficients accounted for streamline curvature. Standard streamline curvature corrections for airfoils, like those in Barlow et al.,[14] assume that, like the airfoil flowfield, the reflected image of the airfoil across the tunnel walls can also be modeled as an infinite wing. Since the relative upwash attributed to streamline curvature was non-uniform across the semispan of the wing, the conventional 2D corrections due to streamline curvature could not be appropriately applied. Alternatively, standard 3D streamline curvature corrections act to correct the measurements for the wing system, but since the wing was non-uniformly loaded, the effects of streamline curvature were not constant across the span. As a result, a different method for correcting the sectional performance for streamline curvature was developed.

The method for correcting the sectional performance was based on the 3D streamline curvature correction in Ewald et al.[15] As discussed in Ewald et al.,[15] if the relative upwash is evaluated at the section quarter-chord, the corrections for streamline curvature at a given location across the span can be applied as changes in effective angle-of-attack and quarter-chord pitching moment coefficient. Values for streamline curvature correction factors were determined for each spanwise section after Ewald et al.[15] A comparison of the resulting corrected and uncorrected lift coefficient for the wing and all three spanwise sections is shown in Fig. 2. From Fig. 2, the corrections made to the sectional performance do appear to be qualitatively consistent with the conventional corrections to the 3D wing data.[13]

Simulated Contamination Configurations

In addition to the clean configuration, five cases of leading-edge contamination were simulated on the NACA 3415 semispan wing. These contamination configurations included a boundary-layer trip on the upper and lower surfaces, two severities of simulated glaze-ice accretions, a simulated rime-ice accretion, and two severities of distributed leading-edge roughness.

The boundary-layer trips were created by calculating the critical roughness height that produced a Re_h of 600. The roughness elements used on the boundary-layer trips were sized just above the resulting critical roughness height. The trips were place at $x/c = 0.01$ on the wing upper surface and at $x/c = 0.05$ on the wing lower surface.

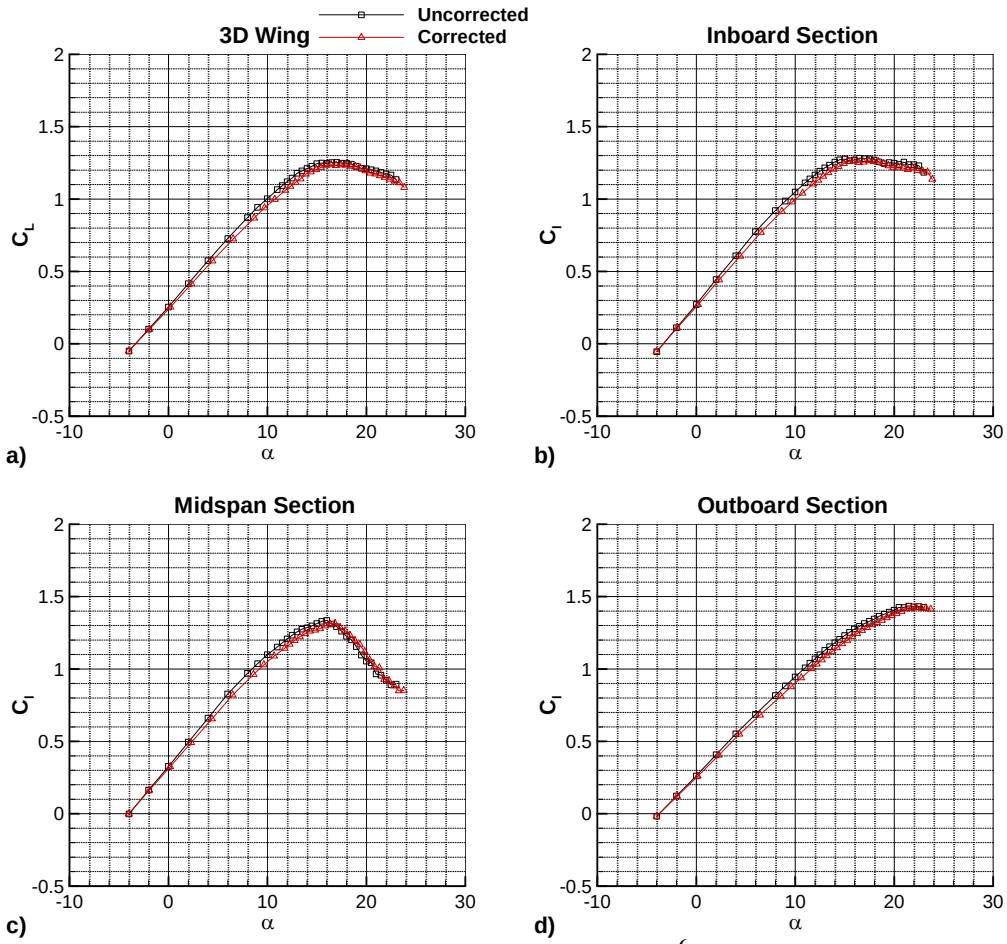

Fig. 2. Corrected and uncorrected lift coefficient at Re = 0.7 × 10^6 and the 0°:0°:0° flap configuration for: a) 3D wing, b) inboard section, c) midspan section, d) outboard section.

Both glaze-ice accretions were simulated using a forward-facing quarter round, which was placed on the model upper surface at x/c = 0.02. The forward-facing quarter round has been used in many previous studies to simulate ice shapes,[8,16,17] and simple geometries have been shown to produce reasonable estimates of ice shape castings by Busch et al.[18] This forward-facing quarter round geometry is representative of a spanwise-ridge ice shape, as described by Bragg et al.[19] In the current investigation, these simulated spanwise-ridge ice shapes are referred to as glaze-ice accretions, since the purpose of using the quarter-round geometry was to provide a representation of a generic glaze-ice accretion, rather than to simulate the aerodynamics of a specific classification of ice shape. The quarter-round geometries for the two glaze-ice accretions had heights measuring 0.1" and 0.05", which were constant across the span. This produced a $h/\bar{c}$ = 0.0144 for the larger simulated glaze ice accretion and a $h/\bar{c}$ = 0.0072 for the smaller simulated glaze ice accretion. The larger simulated shape was denoted as the full glaze-ice case, and the smaller simulated shape was denoted as the half glaze-ice case. A schematic of the full glaze-ice case on the NACA 3415 profile is shown in Fig. 3 a).

The rime-ice accretion was simulated based on the EG1125 streamwise shape in Broeren et al.[20] Like for the glaze-ice case, the streamwise shape was referred to as the rime-ice case in the current investigation, as the purpose of the simulation in the current investigation was to provide a generic representation of a rime-ice accretion, rather than to duplicate a particular classification of ice shape. The shape was created using simple geometry methods similar to those used by Busch et al.[18] As part of the simple geometry simulation, roughness elements were attached to the ice shape, resulting in a roughness $(h/\bar{c})_{avg}$ = 0.0013 across the upper surface from x/c = -0.008 to 0.019 and a roughness $(h/\bar{c})_{avg}$ = 0.00094 across the lower surface from x/c = -0.006 to 0.029. A schematic of the simple geometry rime-ice simulation on the NACA 3415 profile is shown in Fig. 3 b).

The effects of distributed leading-edge roughness were also evaluated on the wing model. The distributed leading-edge roughness was attached to the model using grit in a fashion similar to Ansell et al.[21] The roughness

extended from x/c = 0.01 on the lower surface, and wrapped around the model leading edge up to x/c = 0.07 on the upper surface. Two different severities were tested by using roughness elements of different sizes. The smaller roughness elements installed on the model were composed of 180-grit elements, producing a $(h/\bar{c})_{avg}$ = 0.00043, and the larger roughness elements were composed of 24-grit elements, producing a $(h/\bar{c})_{avg}$ = 0.0039.

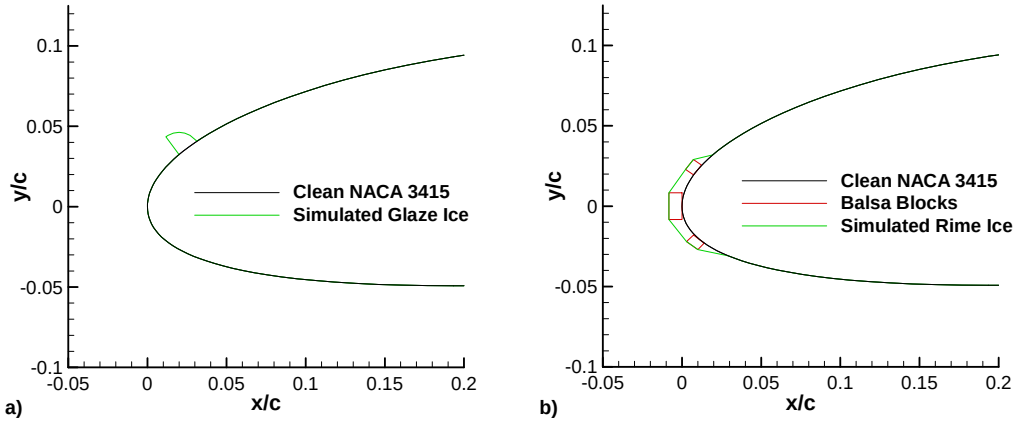

Fig. 3. Schematic of simulated icing cases on NACA 3415 profile: a) glaze-ice case, b) rime-ice case.

Hinge Moment Signal Processing

After hinge moment data were acquired, they were reduced in a fashion similar to that from Ansell et al.[11] Prior to processing, all hinge moment measurements were band-pass filtered between 70 Hz to 260 Hz to reduce the influence of structural frequencies. As in Ansell et al.,[11] three detector functions were used to evaluate the level of hinge moment unsteadiness at each angle of attack in the acquired polar. The first of these detector functions calculated the 4th-order moment about the mean of the unsteady hinge moment signal, and was denoted as the moment function. The second function was based on time-dependent derivatives of the unsteady signal, and was denoted the derivative function. The final function integrated the total spectral content of the hinge moment signal from 70 Hz to 260 Hz, and was denoted the spectrum function.

After calculating the detector function outputs for all angles of attack in the acquired polar, the functions outputs were analyzed with respect to the angle-of-attack margin to the envelope boundary of the corresponding spanwise section, which will be discussed in the following section of this paper. If the relative outputs of the detector functions were consistent between contamination configurations at the same angle-of-attack margins to the envelope boundary, a simple thresholding method could be used to predict and produce an advisory of the approaching envelope boundary, independently of contaminant type. The resulting margins from the three detector functions could then be averaged to produce a more effective prediction of the approaching envelope boundary.

Unsteady Pitch Maneuver

While the initial development of the envelope protection system was performed using data acquired during static airfoil and wing polars, real aircraft operate in a dynamic, maneuvering environment. As a result, these static polars do not simulate the full set of conditions expected for a flight vehicle. A robust envelope protection system must be capable of maintaining reliable protection throughout these types of maneuvers. As a result, the hinge moment reduction system was also tested on the 3D wing while undergoing an unsteady pitching maneuver. The unsteady pitch tests were performed for the wing model in the clean and tripped configuration. As will be shown in the following section, the detector function outputs were relatively comparable across all the roughness-based contamination configurations, with the exception of the rime-ice case. As a result, the tripped configuration provided results that were representative of the other roughness contamination cases. The unsteady pitch maneuvers were conducted for the 0°:0°:0°, 0°:5°:0°, and 0°:-5°:0 flap configurations.

For the unsteady pitch maneuver, the model angle of attack was set to start at α = 7° and pitch up to a final angle of attack of α = 18°, which was above the stall angle of attack of the wing. When sampling, approximately 10 seconds of data were acquired both prior to and after the pitch maneuver. The angle of attack was monitored throughout the pitch maneuver using a potentiometer, which was geared to turn with the balance turntable. The resulting pitch rate of the turntable increased from 0°/s to a maximum of approximately 2°/s. Using this pitch rate of

the turntable, the reduced frequency of the unsteady pitch maneuver was calculated to be $k = 5.035 \times 10^{-5}$. While a higher reduced frequency may have been desirable, the current reduced frequency was produced using the highest pitch rate attainable for the equipment of the current investigation. A higher reduced frequency could have been attained in the current investigation by acquiring measurements at lower test-section speeds, but this was not desired as this would act to reduce the Reynolds number from the static wing tests, and in turn, alter the wing stall characteristics. While this reduced frequency was extremely low and this unsteady pitch maneuver can be easily classified as quasi-steady, it does provide some indication of use of the current system in a dynamic environment. The hinge moments acquired during the unsteady pitch maneuver were reduced through the detector functions across a 1-second sliding window. This length of time for the processing window was shown to be sufficient by studying the time necessary to produce reliable detector function outputs from the static wing hinge moment data.[13] There was a 50% overlap between windows, which corresponded to a 0.5-second overlap. An example showing the pitch maneuver, pitch rate, and inboard and midspan hinge moment coefficients for an unsteady pitch maneuver is shown in Fig. 4.

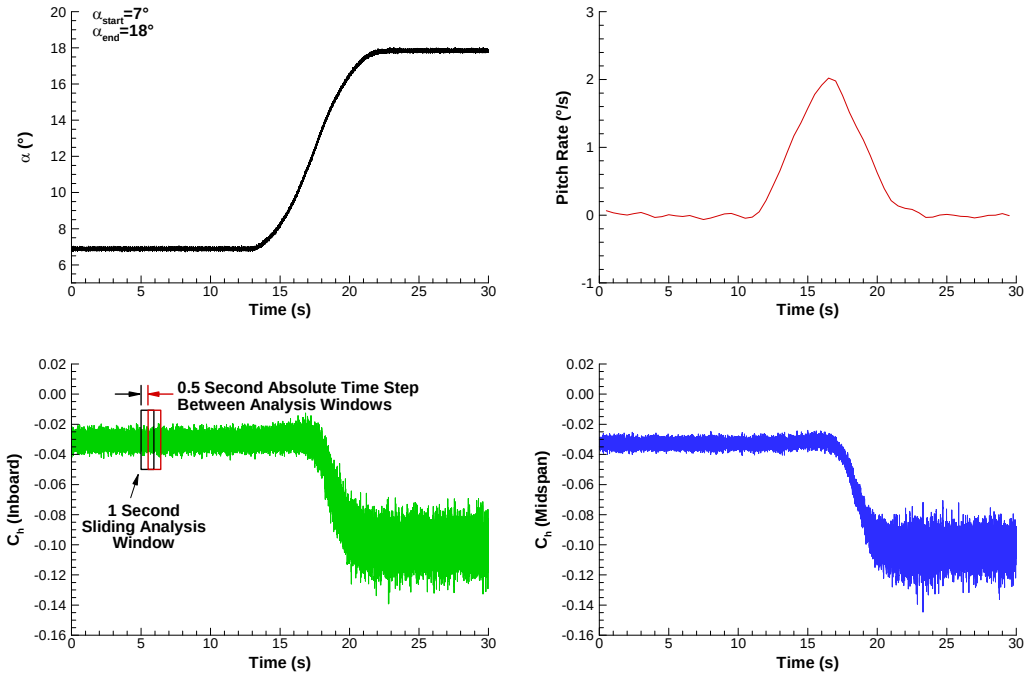

Fig. 4. Example of unsteady pitch maneuver with inboard and midspan hinge moment coefficients.

III. Results and Discussion

The performance of the NACA 3415 semispan wing model obtained from the floor balance measurements in both clean and contaminated configurations is shown in Fig. 5 for $Re = 0.7 \times 10^6$ and the 0°:0°:0° flap configuration. From Fig. 5, the clean wing stalls with $C_{L,max} = 1.24$ at $\alpha_{stall} = 16.4°$. The resulting effects of the simulated contaminants on C_L and α_{stall} at the 0°:0°:0° flap configuration are summarized in Table 2.

As stated in the introduction, the sectional performance characteristics were estimated by integrating surface static pressure measurements and wake profiles taken about the middle of each spanwise section. The resulting sectional performance for the clean wing, compared with the 3D wing performance at the 0°:0°:0° flap configuration is shown in Fig. 6. Also in Fig. 6 are the resulting steady C_h and standard deviation of unsteady C_h measurements for each spanwise section. From Fig. 6, the sectional performance coefficients are qualitatively similar to the 3D wing performance. The only significant difference between the wing performance and the sectional performance is in the difference between C_d and C_D. The wing drag coefficient is significantly higher than the drag coefficient for each of the sections, particularly at higher C_L. However, well after stall the sectional drag coefficients for the inboard and midspan sections become much closer to the wing drag coefficient.

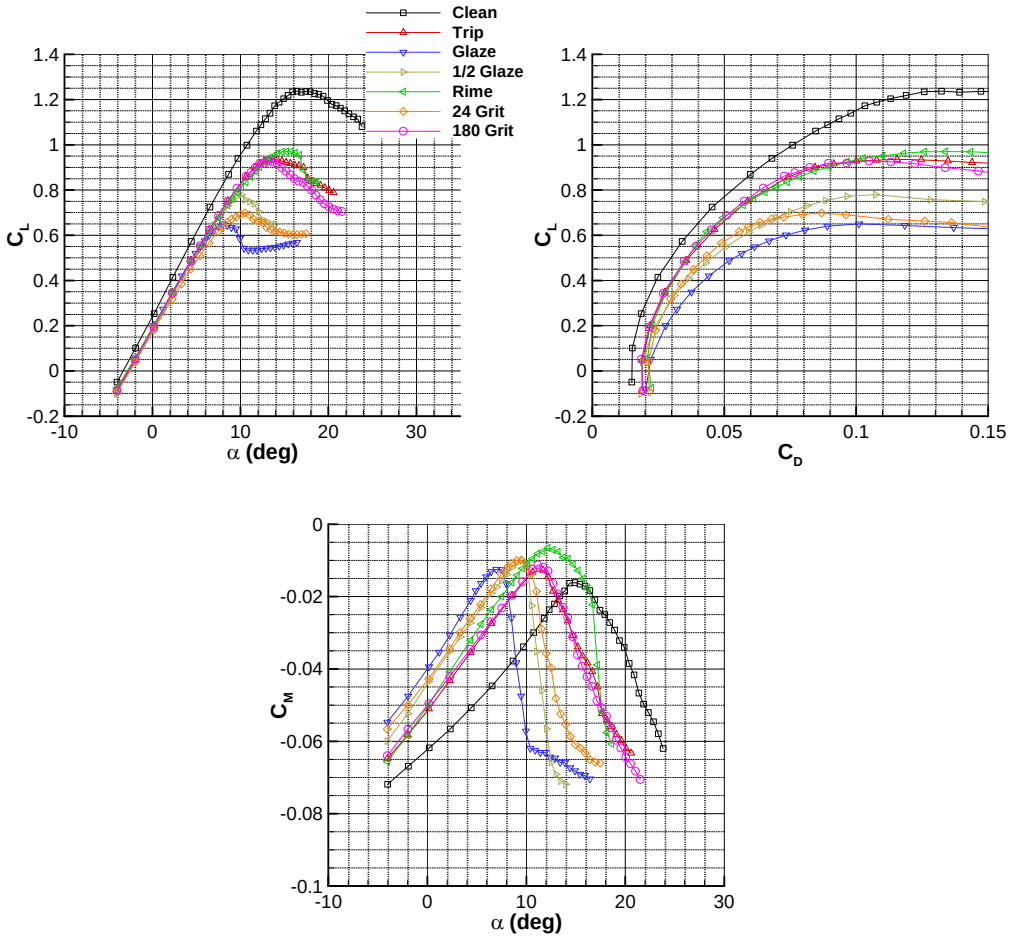

Fig. 5. NACA 3415 wing performance at Re = 0.7 × 10^6 for clean and contaminated configurations for the 0°:0°:0° flap configuration.

	Absolute		Relative	
	$\Delta C_{L,max}$	$\Delta\alpha_{stall}$ (deg)	$\Delta C_{L,max}$	$\Delta\alpha_{stall}$
Clean	--	--	0%	0%
Trip	-0.301	-2.73	-24.4%	-16.6%
Glaze	-0.587	-8.44	-47.5%	-51.4%
½ Glaze	-0.458	-6.35	-37.0%	-38.6%
Rime	-0.267	-1.20	-21.6%	-7.32%
24 Grit	-0.520	-5.40	-42.0%	-32.8%
180 Grit	-0.308	-3.23	-24.9%	-19.7%

(Clean $C_{L,max}$ = 1.237, α_{stall} = 16.43)

Table 2. Summary of contamination effects on C_L for NACA 3415 wing at Re = 0.7 × 10^6 for the 0°:0°:0° flap configuration.

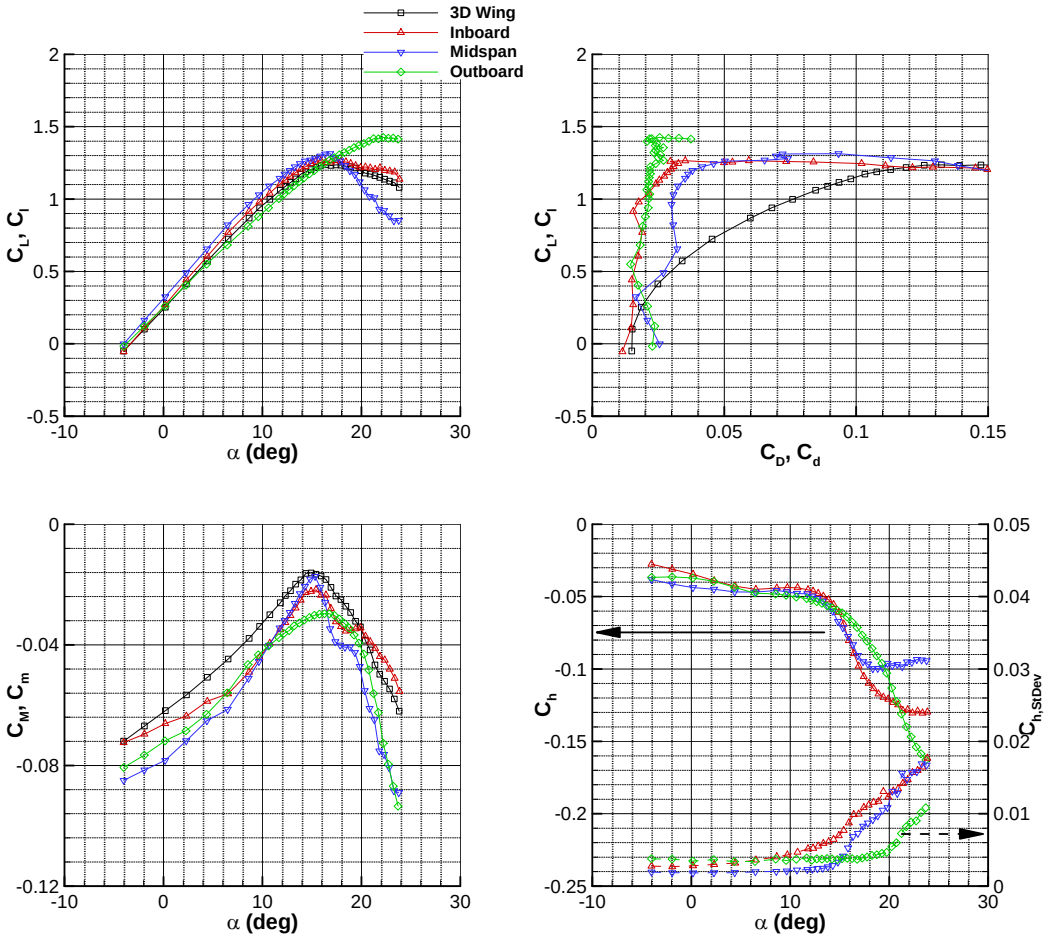

Fig. 6. Comparison of wing performance and sectional performance for clean NACA 3415 wing at Re = 0.7 × 10^6 for the 0°:0°:0° flap configuration.

Surface-oil flow visualization was also performed for the clean wing for the 0°:0°:0° flap configuration in order to obtain a time-averaged image of the wing surface flowfield. The resulting flow visualization is shown, with key flowfield features identified in Fig. 7 for α between 8° and 14°, and in Fig. 8 for α between 14° and 20°. From Fig. 7, at α = 8°, the boundary layer is fully attached over the entire wing, and does not experience any significant three-dimensional effects. However, due to the low Reynolds number, the beginning traces of a leading-edge laminar separation bubble begin forming at α = 10°, along with the first evidence of trailing-edge separation. As α is further increased to 12°, the trailing-edge separation progresses upstream across the midspan section, leading to significant changes in the sectional performance as the midspan section experiences the beginning of a trailing-edge stall. Additionally, the leading-edge laminar separation bubble becomes more discernible, with increased extent along the span of the wing. From Fig. 8, as α is further increased beyond 14°, the trailing-edge separated flow progresses further upstream and across the span. The wing flowfield also experiences significant increases in three-dimensional flow effects. After the wing stalls, for α = 18° and 20°, the flow over the inboard and midspan flaps is completely separated, and most of the flow over the outboard flap is separated. Due to the tip vortex, a small region of flow over the tip of the wing remains attached well past the wing α_{stall}.

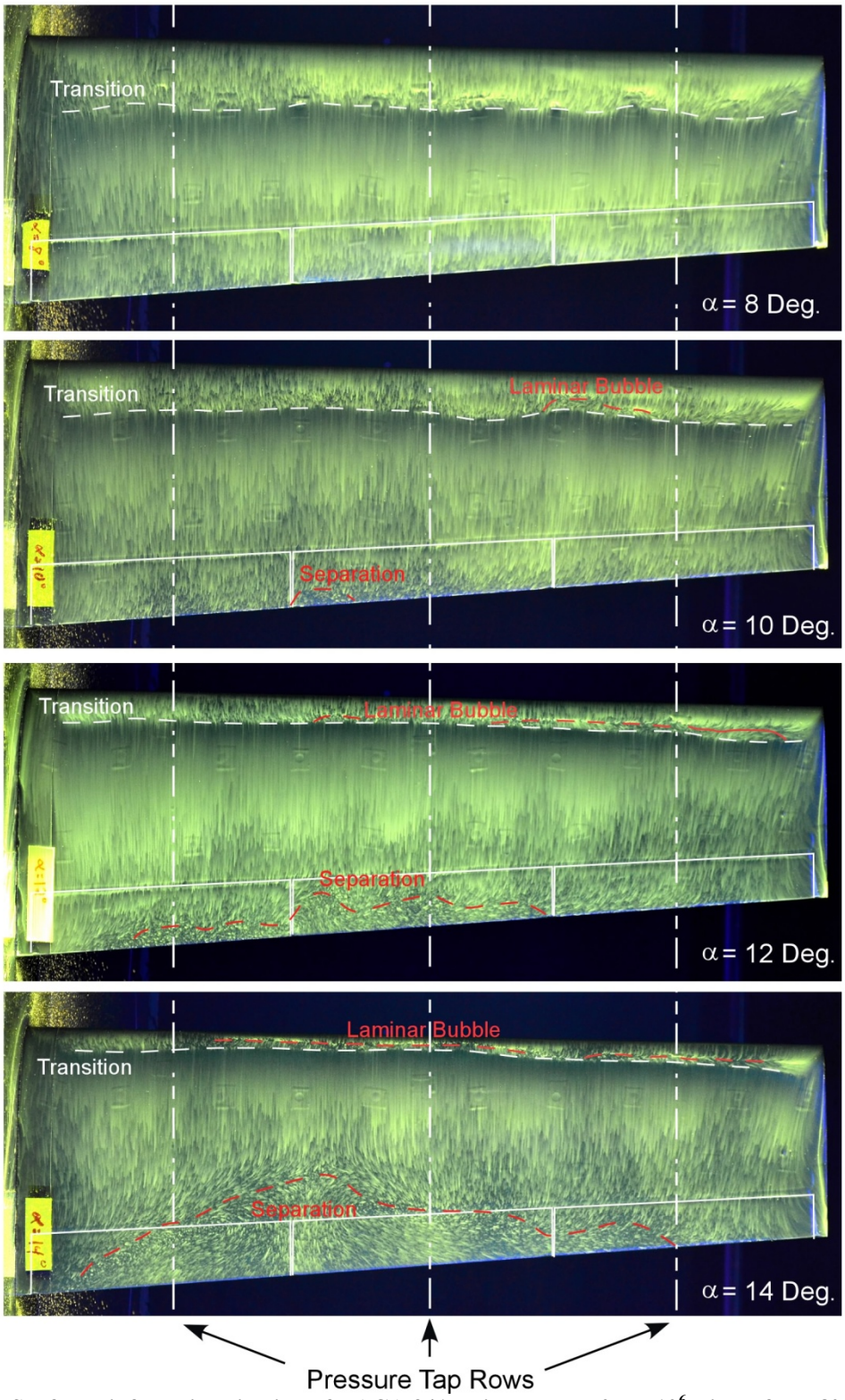

Fig. 7. Surface-oil flow visualization of NACA 3415 wing at Re = 0.7 × 10^6 with α from 8° to 14°.

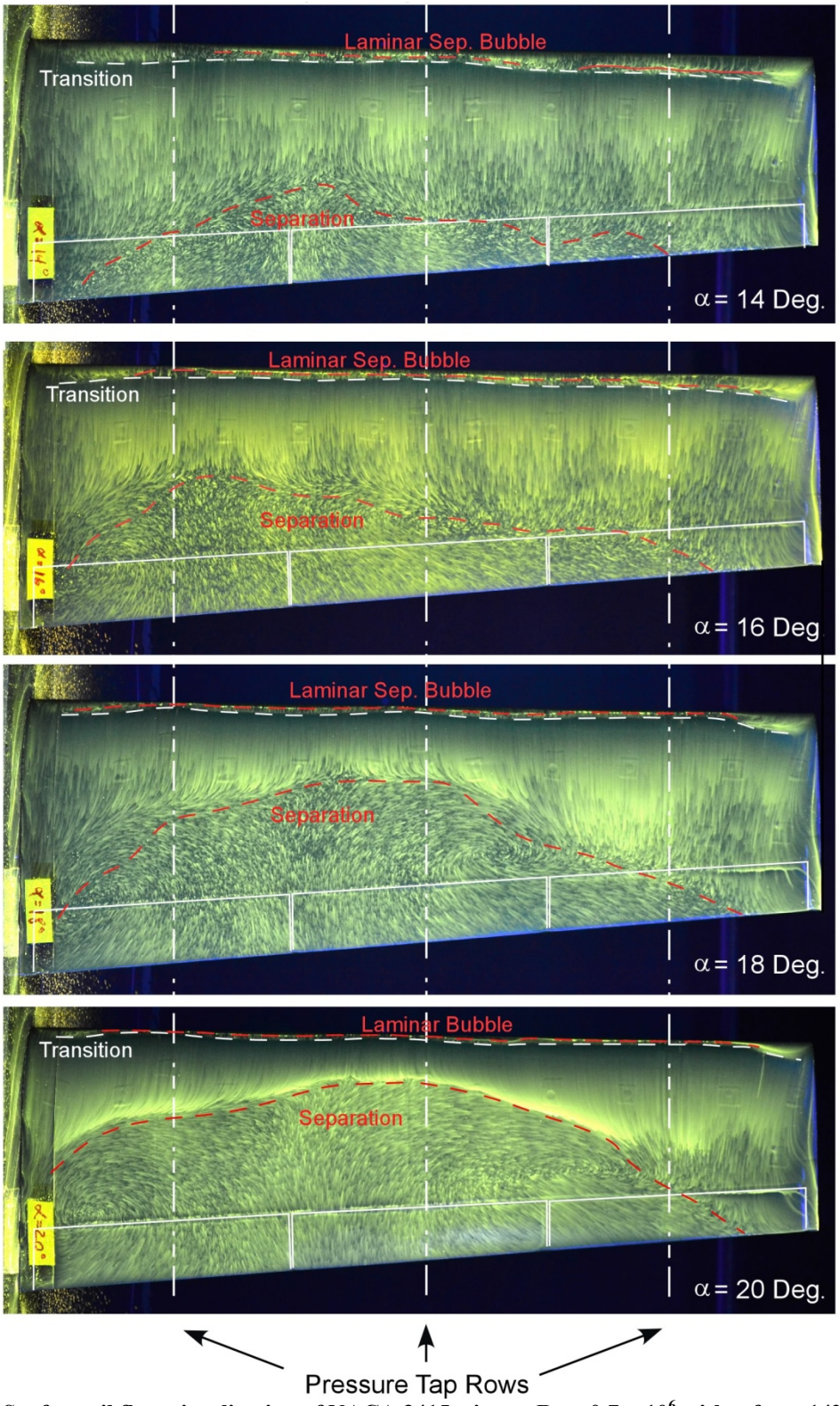

Fig. 8. Surface-oil flow visualization of NACA 3415 wing at Re = 0.7 × 10^6 with *α* from 14° to 20°.

In order for the hinge moment based envelope protection system to be evaluated, the boundary of the envelope had to be determined for each spanwise section and each contamination configuration. The boundary of the adverse aerodynamic envelope was established using the corresponding sectional C_l characteristics. However, stall was not

always very distinct in the sectional lift data, and could not always be used as a criterion for determining the envelope boundary. For the 2D airfoil data used by Ansell et al.,[11] stall was easily identified by a clear break in the lift-curve slope, which was followed by $C_{l,max}$, and a distinct decrease in C_l with a further increase in α. However, in the case of the 3D wing, the sectional C_l does not always have a clearly-defined $C_{l,max}$ followed by a distinct reduction in C_l with increasing α. Instead, for certain cases the sectional C_l would begin to exhibit decreases in slope, and eventually reach a plateau. On occasion, C_l was observed to begin increasing after this plateau, with a subsequent decrease with increasing α. The stall angles of attack for these spanwise sections were not clearly defined, but distinct reductions in sectional performance were visible at well-defined angles of attack where the plateau in C_l was first reached. Since this reduction in sectional performance would represent a deviation from the normal flight envelope, the angle of attack corresponding to the C_l plateau represents the upper α boundary of a normal operating flight envelope for a given spanwise section under the corresponding contamination configuration. This α boundary in the operating envelope will be defined as the critical angle of attack (α_{crit}). Quantitatively, this point can be defined as the angle of attack where the slope of the C_l versus α curve becomes less than 0.01/°. The lift coefficients for the wing and the three spanwise sections, with α_{crit} marked with filled symbols, are shown in Fig. 9.

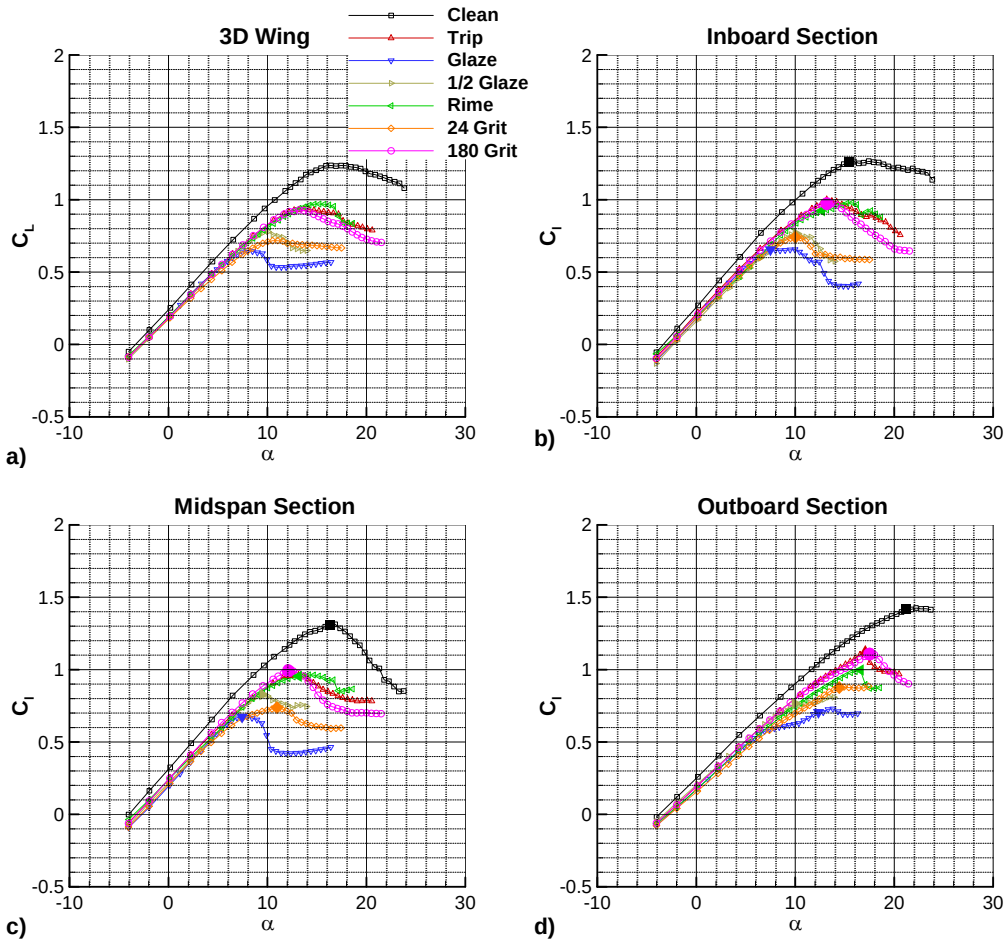

Fig. 9. Lift coefficient vs. α for the 0°:0°:0° flap configuration: a) wing, b) inboard section, c) midspan section, d) outboard section; α_{crit} marked with filled symbols.

After calculating the detector function outputs for each flap across all contamination configurations, the output magnitudes at the same angle-of-attack margin to the envelope boundary (α-α_{crit}) were compared for each spanwise section separately. Since the unsteady hinge moment of each flapped section is processed independently, the aerodynamic state of multiple spanwise sections could be monitored. An example of the detector function outputs for the inboard section as a function of (α-α_{crit}) is presented in Fig. 10.

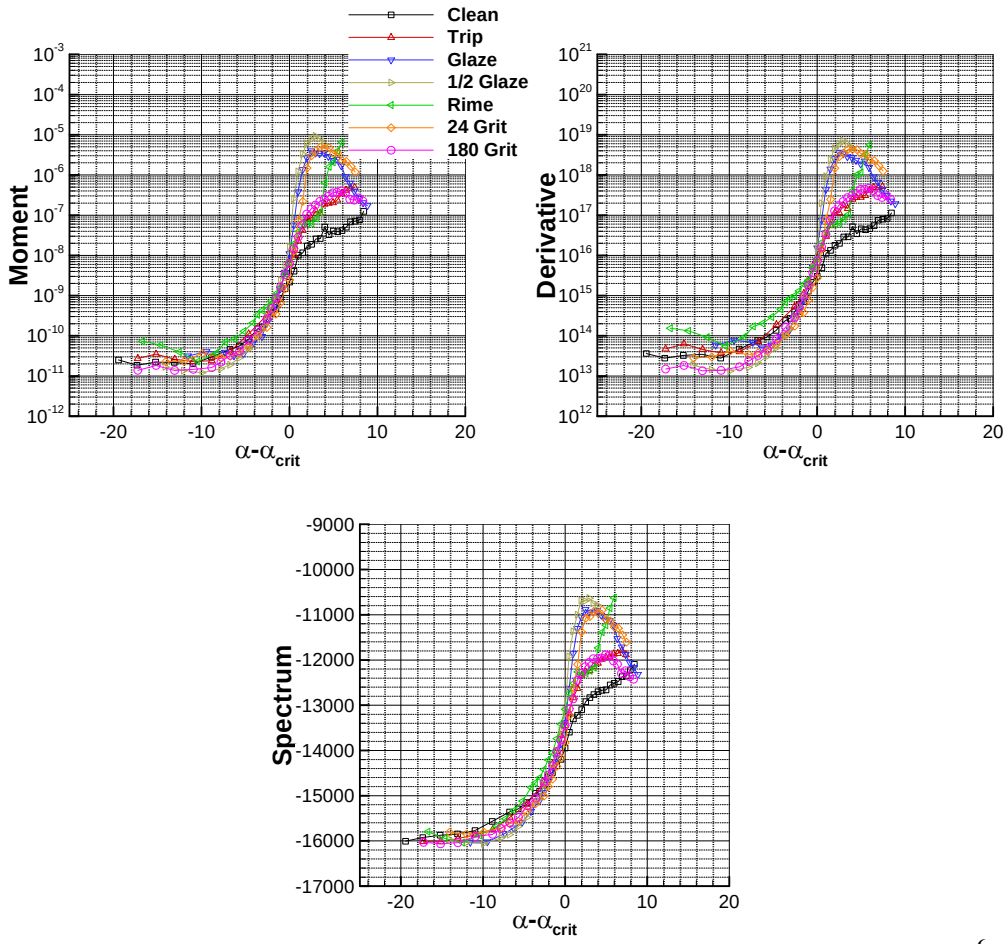

Fig. 10. Detector function output for inboard section of NACA 3415 wing at Re = 0.7 × 10^6, α_{crit} based on plateau in C_l.

From Fig. 10, the resulting hinge moment detector functions appear to provide consistent output levels across the contamination configurations tested when observed as a function of α-α_{crit}. While the output levels for the sectional data of the 3D wing of the current investigation do not collapse to the same output level across contamination configurations quite as well as the 2D airfoil data from the previous investigation by Ansell et al.,[11] the general consistency in output levels would suggest that the same thresholding method could be used to predict the approaching envelope boundary – that is, a threshold value for each of the detector functions is prescribed for a given α-α_{crit} margin. This threshold is used universally across all contamination configurations. Once this threshold value for a detector function output is met or exceeded, an advisory of the approaching envelope boundary can be provided to the flight crew, indicating the spanwise location of the approaching envelope boundary on the wing and estimated angle-of-attack margin to the envelope boundary.

Consistent levels and collapse of the detector function outputs across the contamination configurations were also observed in the inboard and midspan sectional data for the various flap deflections tested in this investigation, with one exception. The clean and the 180-grit roughness cases did not collapse with the other contamination configurations across the midspan section for the 0°:5°:0° flap configuration. The authors believe this can be attributed to the fact that the sectional performance data were derived from one chordwise row of pressure taps, at one spanwise location, to estimate the performance across a finite spanwise section of the wing. Since the unsteadiness in the hinge moment signal was generated from the flowfield across the entire spanwise section of each flap, using the sectional performance measured across the center of the individual spanwise sections, while representative of the sectional performance, does not fully encapsulate the 3D nature of the flowfield of the spanwise section. Upon inspection of the C_l vs. α curves for these two cases, two local maxima in C_l were identified per case. If the local maximum at the higher α were to be used rather than the first local maximum in α, these two cases would collapse well with the other configurations. While these two outlying configurations do exist, they are

of little consequence, as these outlying cases are relatively benign and envelope protection could still be provided for this flap configuration across the contamination configurations of most concern.

Using the resulting detector function outputs for all the contamination configurations tested, a series of exemplary sectional envelope protection warnings were produced at various margins of α-α_{crit}. After calculating the detector function outputs across the entire angle-of-attack range tested, interpolation was used to estimate the actual α-α_{crit} margin at which the threshold value would be met. The α-α_{crit} margins corresponding to each of the three detector functions were then averaged. The error was then calculated between the ideal angle-of-attack margin at which the envelope protection system was set for and the actual angle-of-attack margin at which an advisory would be provided. The resulting calculated error across the flap configurations tested for a desired α-α_{crit} margin of 2° is shown in Fig. 11 for the inboard section and in Fig. 12 for the midspan section.

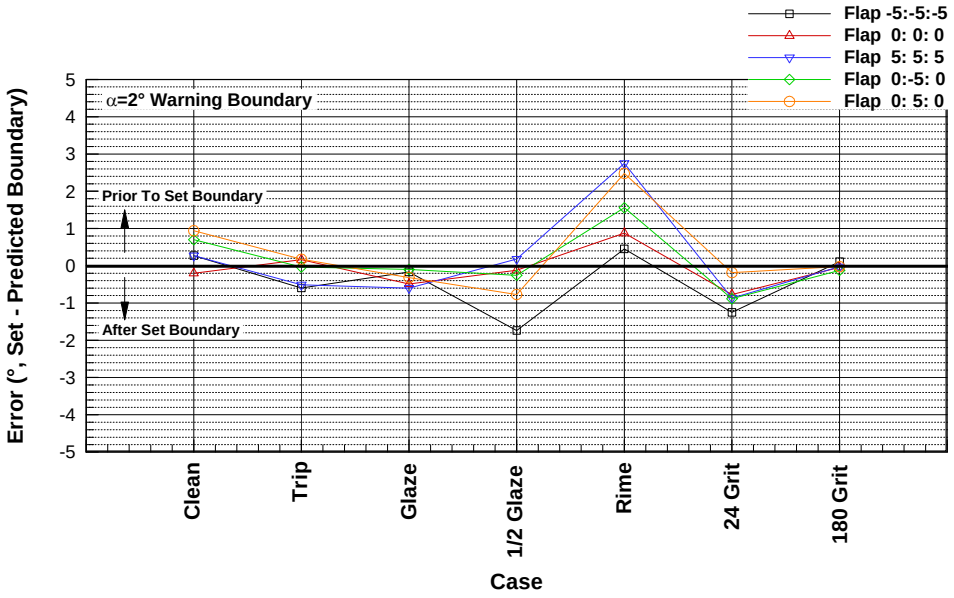

Fig. 11. Average error in inboard section performance advisory prediction for 2° boundary margin across multiple flap settings.

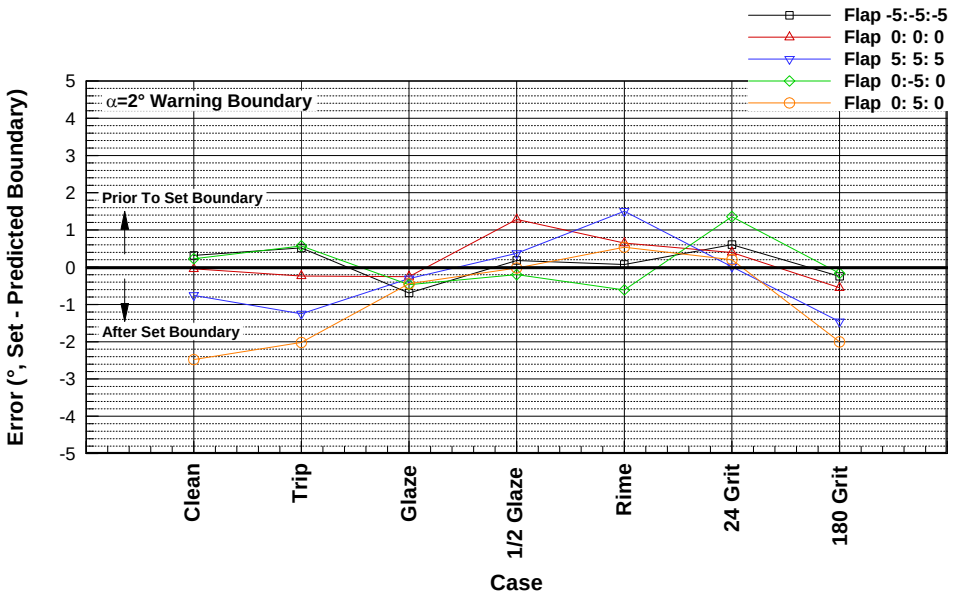

Fig. 12. Average error in midspan section performance advisory prediction for 2° boundary margin across multiple flap settings.

From Fig. 11, the errors between the set and predicted angle-of-attack margin for most cases for the inboard flap are less than ±1°. For the 0°:0°:0° flap configuration, all contamination configurations have error predictions that are less than ±1°. The case with the largest error is the rime-ice configuration, which produces errors from 0.5° before the set boundary up to 2.5° before the set boundary. While these errors are large, they are conservative, and would be provided *prior* to the set α-α_{crit} margin. The other major exceptions are the ½ glaze case and the 24 grit case for the -5°:-5°:-5° flap configuration.

The authors have attributed the large prediction error for the rime-ice case to the difficulty in obtaining good static pressure measurements at the leading edge of the simulated ice shape. Since a simple geometry method was used to simulate the rime ice, this simulated shape blocked many of the model leading-edge pressure taps. Despite efforts that were made to route pneumatic tubing inside of the simulated shape and through the static pressure taps on the model surface, the fidelity of these leading-edge pressure measurements is questionable. Since these static ports record the low leading-edge suction pressures which have a large effect upon the integrated lift coefficient, it is believed that the large error in the predicted rime case boundary is due to the increased uncertainty in the calculated C_l values due to the difficulty in obtaining accurate pressures from these leading-edge ports.

From Fig. 12, the error between the set and predicted angle-of-attack boundaries, for the midspan section at the 0°:0°:0° flap configuration, are slightly larger at approximately ±1.2°. The largest errors were produced by the clean and 180 grit case for the 0°:5°:0° flap configuration. As mentioned previously, this is thought to be due to the use of a single row of pressure taps to estimate the performance of an entire spanwise section. Overall, for the large range of contaminants tested and the wide array of performance effects imposed, the errors in the envelope boundary prediction for the midspan flap were generally within ±1.0° to ±1.2° from the set margin. It is conjectured that if a more accurate integration of the spanwise performance were used over the simple estimation from one row of pressure taps, then these errors are likely to decrease.

Envelope protection advisory predictions were also made for α-α_{crit} margins other than 2° as well. Examples of the resulting calculated errors for various envelope protection margins at the 0°:0°:0° flap configuration are shown in Fig. 13. From Fig. 13, set α-α_{crit} margins from 1° to 3° produce prediction errors of less than ±1° for all of the cases tested with the exception of the ½ glaze case, which produced a prediction error of 1.3° for the 2° set advisory margin. The 4° set advisory margin was shown to produce the largest error, at ±1.3° for the glaze and ½ glaze cases. For all the other cases tested the 4° set advisory margin was also less than ±1°.

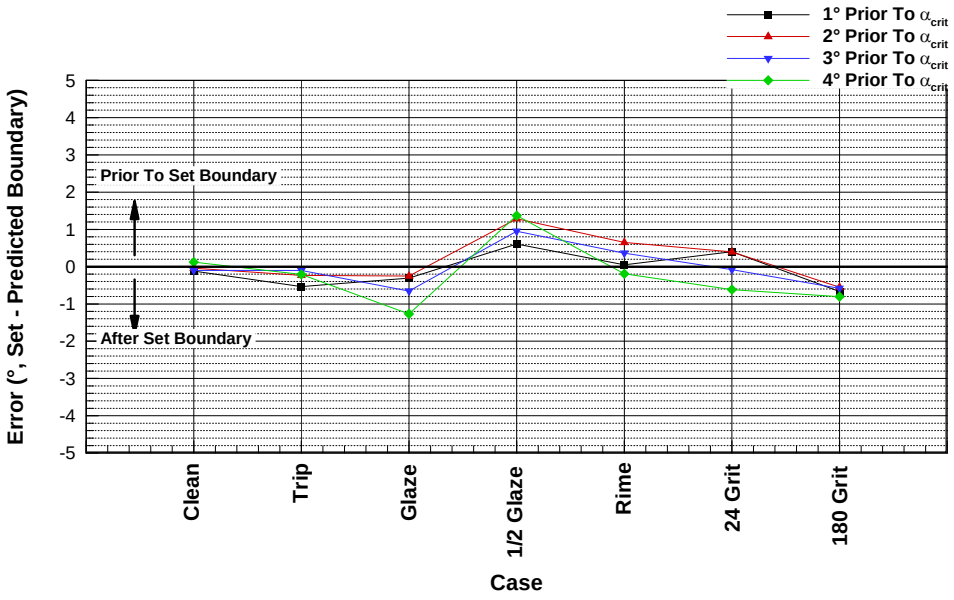

Fig. 13. Average error in midspan section performance advisory for the 0°:0°:0° flap configuration across multiple α-α_{crit} margins.

While the envelope protection advisories produced using the static wing data show that the current envelope protection system can predict the approaching flight envelope boundary with reasonable accuracy for a clean and contaminated wing, it was important to identify changes to the system's efficacy due to unsteady motion. For this reason, hinge moment data were also collected for the wing undergoing an unsteady pitch maneuver. For the sake of

brevity, only the envelope protection results from the midspan flap will be presented for the unsteady pitch maneuver.

An example of the resulting detector function outputs of the midspan flap for the clean case and the 0°:0°:0° flap configuration are shown in Fig. 14, with an α-α_{crit} margin of 2° indicated by the dashed lines. The detector function outputs with respect to time are shown in Fig. 14 a), and the detector function outputs with respect to α-α_{crit} are shown in Fig. 14 b). From Fig. 14 b), the detector function outputs cross the 2° threshold very near an α-α_{crit} margin of 2°. The average error in angle of attack at which this advisory would be provided is 0.05°.

As noted in Section II, the maximum pitch rate during the unsteady pitch maneuver was approximately 2°/sec. This maximum pitch rate corresponds to a reduced frequency of $k = 5.035 \times 10^{-5}$. While this reduced frequency placed the unsteady pitch maneuver well into the quasi-steady classification for unsteady motion, it still provides insight into the effectiveness of the envelope protection system during a gradual maneuver on an aircraft. This shows that the efficacy of the performance advisory system is not significantly affected by the unsteady pitching maneuver of the wing for the clean configuration.

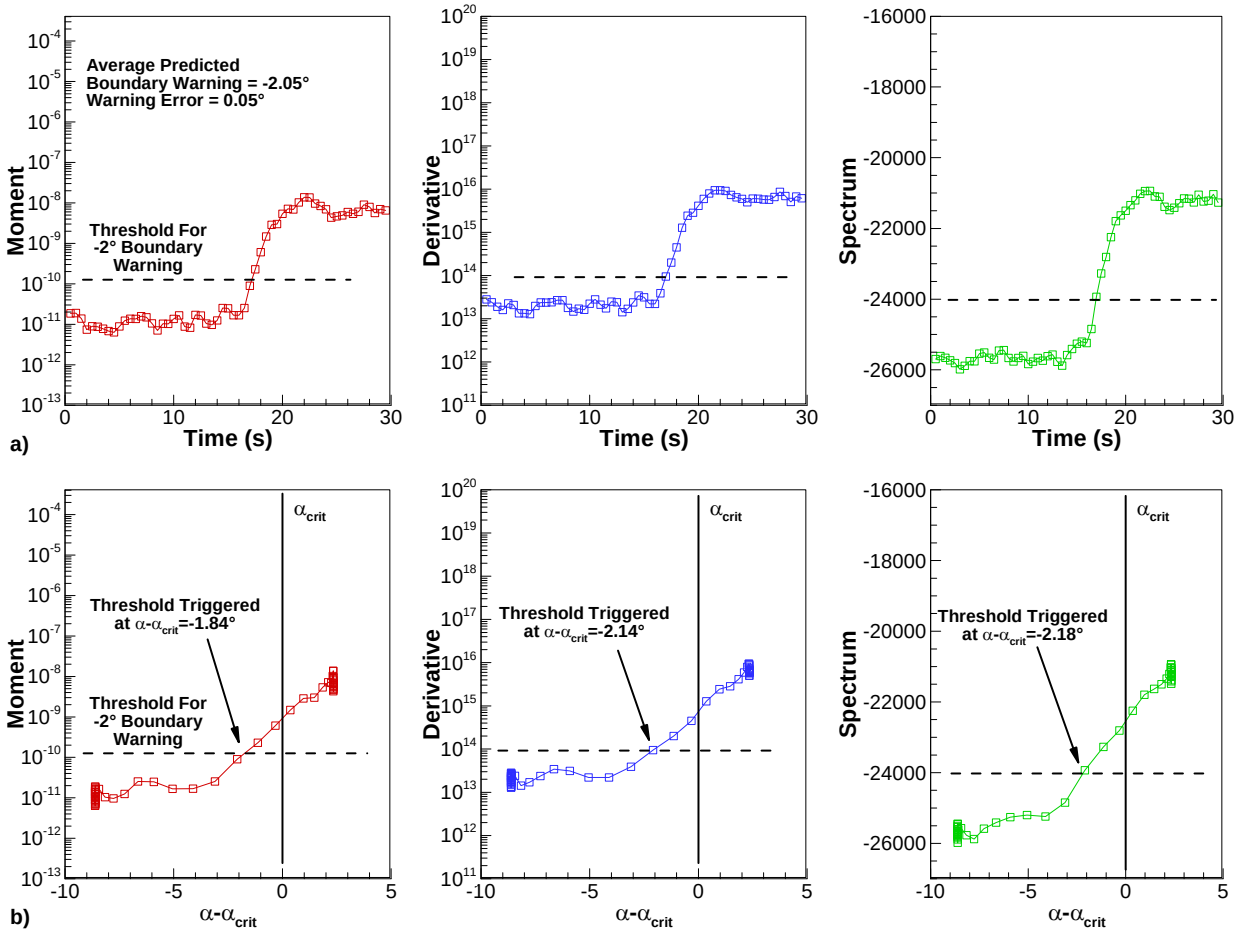

Fig. 14. Detector function outputs of midspan flap for unsteady pitch maneuver with the 0°:0°:0° flap configuration and a 2° α-α_{crit} margin: a) with respect to time, b) with respect to α-α_{crit}.

The resulting envelope protection advisory errors as a function of the individual detector functions, and the average of the three detector functions for the unsteady pitch maneuver for the three midspan flap deflections are shown in Fig. 15 for the clean wing configuration, and in Fig. 16 for the tripped wing configuration. From Fig. 15 and Fig. 16, the envelope protection system performs reasonably well for the 0°:0°:0° and 0°:-5°:0° flap configurations for both the clean and tripped configurations. For the clean case in Fig. 15, the errors in the advisory margin are less than ±0.5°. However, for the 0°:5°:0° flap configuration, the error of the advisory margin increases to 2.8°. The reason for this increase is due to the presence of the two local maxima in C_l for the midspan section for this flap configuration that was reported earlier. As discussed previously, the detector functions for the clean

midspan section did not collapse with the other contamination configurations in the static wing results, and a similar behavior can be observed here.

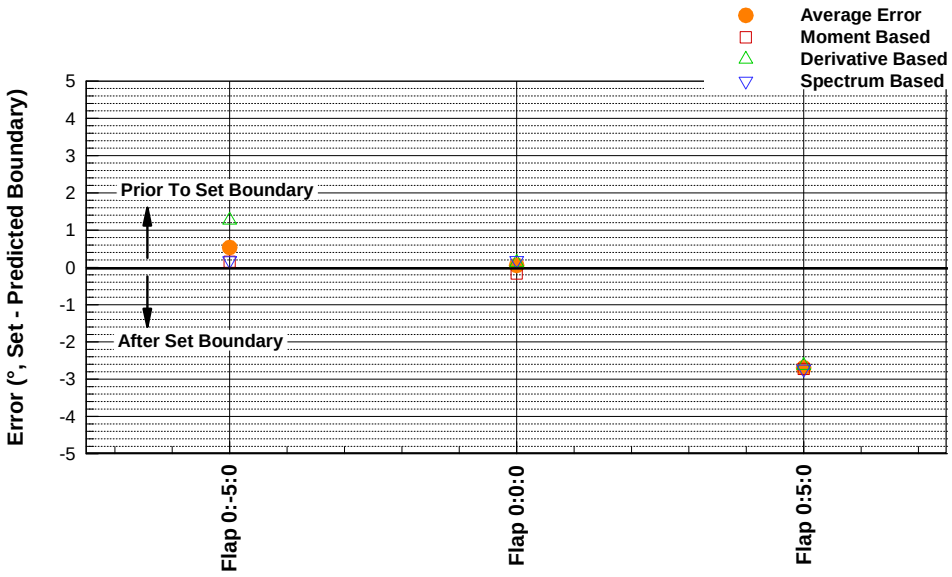

Fig. 15. Average error in midspan section performance advisory prediction for unsteady pitch maneuver of clean wing with 2° α-α_{crit} margin.

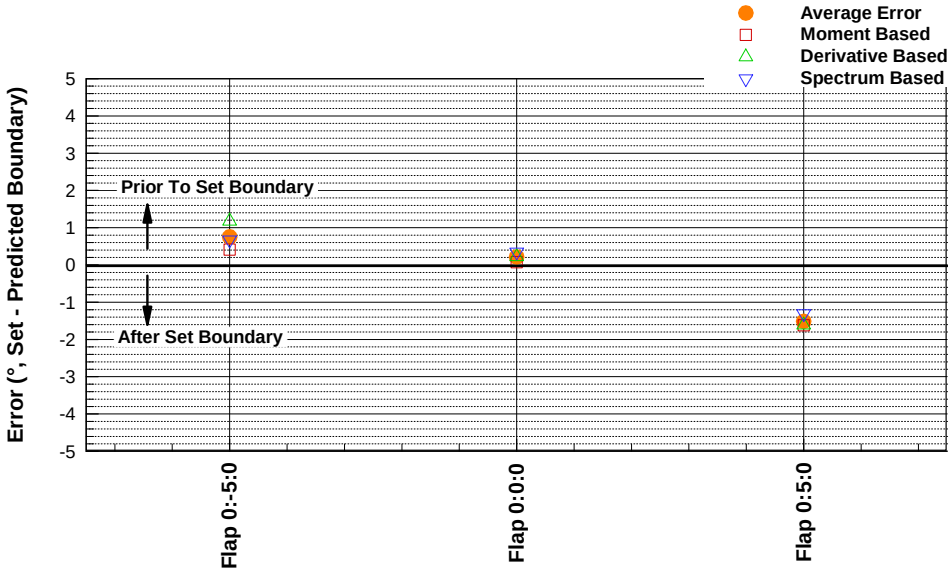

Fig. 16. Average error in midspan section performance advisory prediction for unsteady pitch maneuver of tripped wing with 2° α-α_{crit} margin.

With this outlying flap setting case aside, the envelope protection system shows great potential for providing robust, reliable advisory information to aircraft under clean and contaminated configurations. The expansion of this method from 2D airfoil data to 3D wing data shows that the envelope protection method is capable of providing performance monitoring for independent spanwise sections. As a result, the approaching envelope boundary that can occur due to the presence of contaminants on the leading edge of a wing section, or from exceeding an advised angle of attack, can be predicted. Not only was this method capable of predicting the envelope boundary in sectional performance from data acquired from a static wing polar, but it was also able to predict the approaching

envelope boundary from data acquired during an unsteady pitch maneuver. The few outlying cases could be better resolved by utilizing a better method for obtaining the average sectional performance that is not dependent on a single pressure tap row. Alternative methods for obtaining sectional performance, like pressure-sensitive paint, could provide additional insights into the spanwise structure of the flowfield across a section, and provide a better representation of the performance across a finite spanwise wing section. However, the excellent behavior of the detector functions with the unsteady data is promising for the use of the concept in real-time on a flight vehicle.

IV. Summary and Conclusions

This paper addresses the extension of a hinge moment based envelope protection system, originally developed based on airfoil data, for use on a 3D wing. The system utilizes increases in hinge moment unsteadiness prior to departure from the normal flight envelope for clean and contaminated wing sections in order to predict the approaching flight envelope boundary at a prescribed angle-of-attack margin prior to the event. Unsteady hinge moment data were acquired on an NACA 3415 semispan wing model in a subsonic wind tunnel. In addition to the clean configuration, a number of simulated contamination configurations were also tested. The effects of the simulated contaminants on the wing performance were addressed. Analysis of the hinge moment detector function outputs for an envelope protection advisory indicate that consistent detector function outputs are provided between contamination configurations as a function of α-α_{crit}.

The performance advisory system was also able to reliably predict the approaching envelope boundary across a series of different configurations of flap deflections, with a few exceptions. The authors attribute these exceptions to some of the limitations of the current method for obtaining sectional performance. The envelope protection method was also tested on data from an unsteady pitch maneuver. Results from these limited data suggest that the envelope protection method might also function well in a dynamic environment, in addition to the predictions produced from static wing data.

Overall, the detector functions used for the envelope protection system are shown to be effective, which shows great promise to the future use of the concept in real-time on a flight vehicle. Such a system could be applied to conventional fixed-wing aircraft, but would also be particularly useful for UAV applications where operators remotely piloting these aircraft do not have a "feel" for the aircraft. Similarly, this envelope protection system would be useful for fly-by-wire applications where pilot controls do not have a mechanical linkage to the aircraft control surfaces and unsteadiness in the control surfaces are not mechanically translated to the pilot controls. Further development and implementation of this concept on flight vehicles could offer useful information of the state of the aircraft that would serve as an effective supplement to existing technologies.

Acknowledgements

The authors wish to thank Mark Davis and the staff of NASA Dryden Flight Research Center for their contributions to this work. Support for this program was provided via STTR Contract No. NNX10CB57C.

References

[1] "Statistical Summary of Commercial Jet Airplane Accidents, Worldwide Operations, 1959-2010," Boeing Commercial Airplanes, June 2011.

[2] Wilborn, J.E. and Foster, J.V., "Defining Commercial Transport Loss-of-Control: A Quantitative Approach," AIAA-2004-4811, *AIAA Atmospheric Flight Mechanics Conference and Exhibit*, Providence, RI, August 2004.

[3] Belcastro, C.M., and Foster, J.V., "Aircraft Loss-of-Control Accident Analysis," AIAA-2010-8004, *AIAA Guidance, Navigation, and Control Conference*, Toronto, Ontario Canada, August 2010.

[4] Busch, G.T., Broeren, A.P., and Bragg, M.B., "Aerodynamic Simulation of a Horn-Ice Accretion on a Subscale Model," *AIAA Journal of Aircraft,* Vol. 45, No. 2, 2008, pp. 604-613.

[5] Fedele, J., private communication, 15 June 2011.

[6] Luers, J. and Haines, P., "Heavy Rain Influence on Airplane Accidents," *AIAA Journal of Aircraft,* Vol. 20, No. 2, 1983, pp. 187-191.

[7] Broeren, A.P. and Bragg, M.B., "Effect of Airfoil Geometry on Performance with Simulated Intercycle Ice Accretions," *AIAA Journal of Aircraft*, Vol. 42, No. 1, 2005, pp. 121-130.

[8] Gurbacki, H.M. and Bragg, M.B., "Sensing Aircraft Icing Effects by Unsteady Flap Hinge-Moment Measurement," *AIAA Journal of Aircraft,* Vol. 38, No. 3, 2001 pp. 575-577.

[9] "Aircraft Surface Contamination Sensing System Using Control Surface Hinge Moment Measurements," M.B. Bragg and H. M. Gurbacki, patent # 6,140,942, October 31, 2000.

[10] Bragg, M.B., Basar, T., Perkins, W.R., Selig, M.S., Voulgaris, P.G., Melody, J.W., and Sarter, N.B., "Smart Icing Systems for Aircraft Icing Safety," AIAA-2002-0813, *AIAA Aerospace Sciences Meeting & Exhibit*, Reno, NV, Jan. 2002.
[11] Ansell, P.J., Bragg, M.B., and Kerho, M.F., "Stall Warning Using Flap Hinge Moment Measurements," *AIAA Journal of Aircraft*, Vol. 48, No. 5, 2011, pp. 1822-1824.
[12] Kerho, M.F., Bragg, M.B., Ansell, P., and Kramer, B.R., "Final Report; Real-Time Control Surface Hinge Moment Measurements for Novel Flight Envelope Monitoring System," Phase I STTR Final Report, Contract No. NNX09CF549.
[13] Kerho, M.F., Bragg, M.B., Ansell, P., and Kramer, B.R., "Final Report; Real-Time Control Surface Hinge Moment Measurements for Novel Flight Envelope Monitoring System," Phase II STTR Final Report, Contract No. NNX10CB57C.
[14] Barlow, J. B., W.H. Rae, J., and Pope, A., *Low-Speed Wind Tunnel Testing*, John Wiley & Sons, Inc., NY, 3rd ed., 1999.
[15] Ewald, B.F.R., et al., "Wind Tunnel Wall Correction," AGARDograph 336, published by the North Atlantic Treaty Organization, October 1998.
[16] Lee, S., Bragg M. B., "Experimental Investigation of Simulated Large-Droplet Ice Shapes on Airfoil Aerodynamics," *AIAA Journal of Aircraft*, Vol. 36, No. 5, 1999, pp. 844-855.
[17] Broeren, A. P., Whalen, E. A., Busch, G. T., and Bragg, M. B., "Aerodynamic Simulation of Runback Ice Accretion," AIAA-2009-4261, *1st AIAA Atmospheric and Space Environments Conference*, San Antonio, TX, June 2009.
[18] Busch, G. T., Broeren, A. P., and Bragg, M. B., "Aerodynamic Fidelity of Sub-scale Two-Dimensional Ice Accretion Simulations," AIAA-2008-7062, *26th AIAA Applied Aerodynamics Conference*, Honolulu, HI, Aug. 2008.
[19] Bragg, M.B., Broeren, A.P., and Blumenthal, L., "Iced-Airfoil Aerodynamics," *Progress in Aerospace Sciences*, Vol. 41, No. 5, 2005, pp. 323-362.
[20] Broeren, A. P., Bragg, M. B., Lee, S., Moens, F., and Guffond, D., "Effect of High-Fidelity Ice Accretion Simulations on the Performance of a Full-Scale Airfoil Model," AIAA-2008-434, *46th AIAA Aerospace Sciences Meeting and Exhibit*, Reno, NV, Jan. 2008.
[21] Ansell, P.J., Bragg, M.B., and Kerho, M.F., "Envelope Protection System Using Flap Hinge Moment Measurements," *28th AIAA Applied Aerodynamics Conference*, Chicago, IL, June 2010.